Research Article Vol. 32, No. 4 / 12 Feb 2024 / Optics Express 5885

Optics EXPRESS

Holographic imaging of antiferromagnetic domains with in-situ magnetic field

JACK HARRISON,[1] HARIOM JANI,[1,2,5] JUNXIONG HU,[2] MANOHAR LAL,[3] JHENG-CYUAN LIN,[1] HORIA POPESCU,[4] JASON BROWN,[1] NICOLAS JAOUEN,[4] A. ARIANDO,[2] AND PAOLO G. RADAELLI[1,6]

[1] *Clarendon Laboratory, Department of Physics, University of Oxford, Oxford, OX1 3PU, UK*
[2] *Department of Physics, National University of Singapore, Singapore*
[3] *Department of Electrical and Computer Engineering, National University of Singapore, Singapore*
[4] *Synchrotron SOLEIL, L'Orme des Merisiers, Saint-Aubin, B.P. 48, 91192 Gif-sur-Yvette, France*
[5] *hariom.jani@physics.ox.ac.uk*
[6] *paolo.radaelli@physics.ox.ac.uk*

Abstract: Lensless coherent x-ray imaging techniques have great potential for high-resolution imaging of magnetic systems with a variety of in-situ perturbations. Despite many investigations of ferromagnets, extending these techniques to the study of other magnetic materials, primarily antiferromagnets, is lacking. Here, we demonstrate the first (to our knowledge) study of an antiferromagnet using holographic imaging through the 'holography with extended reference by autocorrelation linear differential operation' technique. Energy-dependent contrast with both linearly and circularly polarized x-rays are demonstrated. Antiferromagnetic domains and topological textures are studied in the presence of applied magnetic fields, demonstrating quasi-cyclic domain reconfiguration up to 500 mT.

1. Introduction

Synchrotron-based x-ray imaging has become an invaluable tool for the study of magnetic, quantum and functional materials for a wide variety of fundamental and application-based research. X-ray photoelectron emission microscopy (X-PEEM), scanning transmission x-ray microscopy (STXM) and several other related techniques have been successfully employed to study a wide range of materials with spatial resolutions down to a few tens of nm [1–5]. All of these methods rely on core-level spectroscopy to produce contrast, but differ in the way the image is created. The availability of appropriate sample environments to apply *in-situ* perturbations to the sample is of great importance to enhance the impact of this research, and much progress has been made to provide non-standard environments and stimuli [6–8].

In this respect, many x-ray based imaging techniques suffer from fundamental limitations, which restrict the complexity of the sample environment and consequently the accessible phase space. For transmission-based techniques such as STXM, the limitation is geometrical and relates to the requirement for focusing optics very close to the sample [1]. In the case of X-PEEM, large voltage differentials at the sample stage are required to extract and accelerate secondary electrons, significantly limiting the available space around the sample [9]. Moreover, the very nature of the X-PEEM technique, which is based on charged particles, makes it difficult to image samples in large applied magnetic or electric fields. As an alternative, photon-based lensless imaging is particularly appealing, since the x-ray beam does not need to be focused, freeing up space around the sample, and no distortion is introduced when fields are applied [10]. The traditional difficulty with such techniques has been the limited availability of a coherent x-ray beam, but this is being progressively overcome by modern synchrotron designs, which provide large coherent

#508005 https://doi.org/10.1364/OE.508005
Journal © 2024 Received 11 Oct 2023; revised 12 Jan 2024; accepted 15 Jan 2024; published 5 Feb 2024

fractions in the soft x-ray regime. A further boost to techniques based on bright coherent sources will be provided by fourth-generation storage rings based on the multi-bend achromat lattice concept [11,12], as well as x-ray free electron lasers [13]. In this context, it is worth emphasising that full-field lensless methods do not require scanning, and are therefore ideal for time-resolved studies.

X-ray Fourier transform Holography (FTH) is a family of related lensless imaging techniques, all aiming to reconstruct a real space, full-field image of a sample by performing an inverse Fourier transform on a measured interference pattern between the sample and a reference structure [14]. Unlike STXM and related techniques such as ptychography [1,15], FTH does not rely on close-in imaging optics. This creates greater flexibility for sample environment and external stimuli [10], and also means that the fundamental resolution of the technique is limited by the x-ray wavelength and precision of the reference structure, rather than the resolution of the employed optics in STXM, and can therefore be better by up to an order of magnitude. This also does not require complicated and computationally expensive phase retrieval algorithms as in ptychography. The main drawback of FTH is the need to create an x-ray mask, including a reference with feature sizes that are comparable to the resolution one wants to obtain, which requires a significant investment in nanofabrication. A recent development suggests that the resolution of holographic techniques can be improved further through phase retrieval algorithms, if the mask is designed with this goal in mind [16].

Within the FTH family, holography with extended reference by autocorrelation linear differential operation (HERALDO) [17,18] is a variant of standard holographic techniques that uses an extended shape (such as a slit) as the scattering reference that interferes with the diffraction from the object under study. Both the sample and the reference are defined by a strongly x-ray absorbing mask, into which an object hole and the reference object are cut. A suitable linear differential filter is applied to a measured far-field interference pattern, such that the inverse Fourier transform of the resulting diffraction pattern generates several real-space reconstructions of the object (see Fig. 1(a)) [19–22]. HERALDO has several advantages over standard FTH. Firstly, the flexibility to manufacture general shaped references rather than the small holes required by standard FTH allows for enhanced flexibility in sample geometry and manufacturing processes [17,18]. As the extended references have greater x-ray transmission than hole references for FTH, lower photon fluxes are required for comparable image quality. HERALDO can also be used to reconstruct 3D tomographic structures by rotating the sample about an axis parallel to the slit [23]. Finally, the resolution of HERALDO is determined by the size of the sharpest corner one can manufacture, rather than the overall size of the reference hole, meaning that it can be in principle up to an order of magnitude finer [19]. Since its original development, HERALDO has been mainly employed to image ferromagnetic materials through circular dichroism [14,19–22]. As discussed further below, HERALDO images can be created by exploiting many different contrast mechanisms, and it is therefore suitable to study a much wider class of materials than conventional ferromagnets.

1.1. Magnetic and topological textures in α-Fe_2O_3

α-Fe_2O_3 is a quasi-collinear canted antiferromagnet (AFM) which has been studied for decades as a model magnetic system. More recently, it has been identified as a candidate for applications in spintronics, due to its long-range spin diffusion, reasonably large spin-Hall magnetoresistance, low Gilbert damping and widely tunable magnetic anisotropy [24–29]. α-Fe_2O_3 has a high Néel temperature ($T_N \approx 950\,K$ in bulk samples); its topological properties stem from the unusually low magnetic anisotropy, which changes sign from in-plane (IP) to out-of-plane (OOP) upon cooling through the so-called Morin transition ($T_M \approx 260\,K$ in bulk samples) [30,31]. Other than very close to T_M, the basal-plane anisotropy is orders of magnitudes smaller than the axial anisotropy, meaning that the different in-plane spin directions are almost identical energetically. This favors complex in-plane spin patterns, which are strongly reminiscent of Schlieren textures

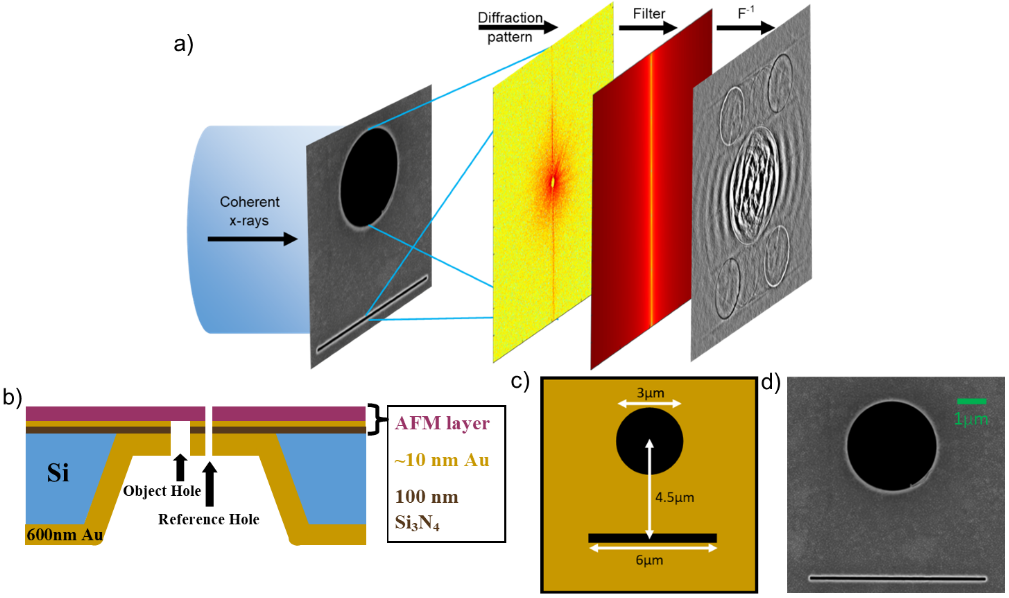

Fig. 1. a) Schematic of HERALDO technique. A coherent X-ray beam illuminates an object hole and slit, leading to an interference pattern. The application of a linear filter and recreation of the final image through an inverse Fourier transform are also shown. b) Cross-section diagram of our masks (not to scale) with sample post-transfer, highlighting the various layers and the milling structure. c) Diagram of object hole and reference slit layout with relevant dimensions. d) Scanning electron microscope image of an example hole/slit in our holography mask after preparation in FIB but before sample application.

in liquid crystals and can have similar topological characters. Moreover, α-Fe_2O_3 has a weak ferromagnetic moment above the Morin transition due to a small in-plane canting of the two sublattices towards each other, thereby allowing the antiferromagnetic domains to weakly couple to an applied field [30,31].

Very recently, interest in α-Fe_2O_3 has been rekindled thanks to the discovery that this system can host topological magnetic textures (merons, antimerons and bimerons) at room temperature, making it a potential platform for racetrack-based spintronic devices and other unconventional computing paradigms [3,29,32–34]. These studies exploited energy-dependent linear-dichroic x-ray absorption (referred to as energy-XMLD contrast) to image antiferromagnetic domains and topological textures in both thin films [3,32] and free-standing membranes [34]. We demonstrated therein that topological textures can be repeatedly nucleated by a first-order analogue of a Kibble-Zurek transition [35–37]. In spite of the promising results obtained on α-Fe_2O_3 by X-PEEM and STXM, a bottleneck in research has been the inability to apply steady-state in-situ perturbations, such as magnetic fields, in combination with imaging. For example, although we were able to demonstrate that sufficiently large *ex-situ* magnetic fields result in bimeron annihilation whilst preserving the non-topological characters of the AFM domain structure [32], we were not able to image the sample whilst this process was unfolding due to the aforementioned limitations of the technique. Such *in-situ* field investigations are crucial as our recent study has unveiled that topological AFM textures in α-Fe_2O_3 host monopolar, dipolar and quadrupolar *emergent* magnetic charge distributions coupled to the AFM order [38], enabling their direct manipulation via Zeeman interaction.

Following our recent success in growing free-standing α-Fe_2O_3 membranes hosting topological textures, which are suitable for imaging in transmission [34], we are now able to overcome this limitation using the HERALDO scheme in energy-XMLD contrast mode. In this paper, we employ HERALDO to image antiferromagnetic domain structures (for the first time, to our knowledge), including topological textures, in α-Fe_2O_3. We employ both energy and linear dichroic (XMLD) contrast to image the full director field associated with the spatial variation of the Néel vector. We also demonstrate that these textures can be manipulated by *in-situ* application of steady-state magnetic fields up to 800 mT, both above and below T_M, further emphasising the role that FTH methods can play in the study of extended phase diagrams. Furthermore, we show that circularly polarized x-rays can be used to produce HERALDO images of magnetic antiphase domain walls (ADWs) below T_M, despite the commonly held belief that circularly-polarized x-rays cannot be used to probe antiferromagnetic order [32,39,40].

2. Materials and methods

2.1. Sample preparation

The resolution of HERALDO is primarily determined by the size of the reference corners that correspond to the reconstructions, i.e., how carefully and precisely one can prepare the mask. In addition, as the mask will never be perfectly x-ray absorbing, the overall contrast of the technique is determined by the relative x-ray transmission of the object relative to the mask. There are also a set of criteria that determine the relative object-reference sizes and spacing to ensure that different reconstructions do not overlap [17,18]. This effectively shifts the experimental difficulties usually associated with beamline operation to the sample and mask preparation, thereby allowing for greater flexibility in the experimental chamber itself [10].

To prepare the mask, we used commercial (Silson) holders made of 100 nm thick Si_3N_4 membranes mounted on 5 mm x 5 mm x 0.5 mm Si substrates with a 1 mm x 1 mm window cut out as a base. The mask was grown via e-beam evaporation of Au wire using an Edwards EB3 electron gun. The chamber was evacuated to a base pressure of 1.2×10^{-5} mbar. A 600 nm Au layer was evaporated at a rate of 0.25 nm/s using a 55 mA beam current. As Au has a typical x-ray attenuation length of 60 nm in the energy range of interest (700-800 eV) [41], we expect a mask transmission of approximately 1/2000 of the incident intensity, which should be sufficient to ensure a reasonable contrast. Moreover, about $\approx$10 nm of Au was coated on the reverse of the membrane to make the surface conductive for the further processing steps described below.

After Au coating, the masks were mounted in a FEI/ThermoFisher Nova 600 NanoLab DualBeam FIB/SEM to perform the milling. An ion beam voltage of 30 kV and beam current 28 pA was used to mill both the slits and holes. These values were optimized to make the slits as narrow and uniform as possible in order to minimize spurious reconstructions and maximize attainable resolution. We milled a 10x3 array of 3 μm diameter holes separated by 50 μm. Along with each hole, an associated slit was milled 4.5 μm from the center of the hole. Slits were 6 μm long and slightly off-center (to aid with the filter application algorithm). These are shown schematically and as imaged in a scanning electron microscope in Fig. 1(b)-(d). These dimensions ensure that all the reconstruction separation criteria are satisfied. The milled slits had a width between 40 nm and 70 nm, indicating that this is the best resolution we would expect to achieve. This is confirmed in Fig. 2(a),(b), wherein linecuts of example domain walls suggest a resolution close to 30 nm as will be explained further in section 3.1.1. The array of multiple holes, whose inter-hole separation was larger than the beam size, allowed us to explore different regions of the sample by moving it relative to the beam on a motorized stage. This helped to overcome the limited field of view that is otherwise a downside of this technique.

(001)-oriented, 30 nm thick α-Fe_2O_3 membranes were prepared by pulsed laser deposition growth on $SrTiO_3$ substrates with a water-soluble $Sr_3Al_2O_6$ (SAO) layer and a (111)-oriented $SrTiO_3|LaAlO_3$ buffer to enhance the crystalline quality of the films. These membranes were transferred onto the prepared sample holders by using a lift-off and targeted transfer technique after water-etching the SAO layer; for full details of the preparation process and sample characterization

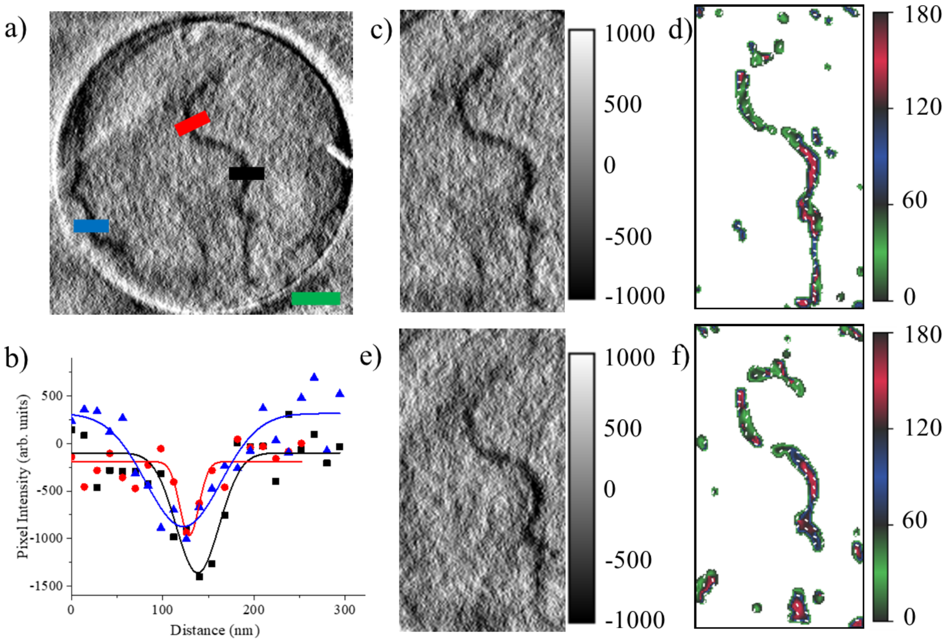

Fig. 2. (a) Holographic image of an AFM domain wall and (b) a set of linecuts taken across that domain wall along with corresponding Gaussian fits of the intensity, demonstrating the resolution achieved with this technique. (c,e) Holographic E-XMLD images and (d,f) vector maps taken at 280 K (below T_M) across the ADW shown in (a). (c,d) are in the absence of an applied field and (e,f) are with a constant 650 mT field applied towards the right of the image. Green scale bar in (a) is 500 nm. Red-green-blue colors and white bars represent fitted Néel vector orientation, with the angle measured relative to the vertical axis shown by the scale bar.

see [34]. The targeted transfer technique used herein minimized bent or crumpled regions and the object holes used for imaging were confirmed to be absent of large structural defects via optical imaging (see Fig. S3). The buffer layer remains attached to the α-Fe$_2$O$_3$ post-transfer, but has no effect on the magnetic properties of the film [34]. To re-mill the slits, we used a focused beam of Neon ions in a Zeiss Orion NanoFab (He/Ne ion Microscope). We used a beam current of 5 pA, ion beam energy of 26 KeV, a dose of 3.5×10^{17} ions/cm^2, and a fixed dwell time of 25 µs. An area 7 μm x 0.4 μm was milled about each slit in a raster scan with a beam spacing 1 nm x 1 nm. This removed all of the sample and buffer layer covering the slits, thereby ensuring that x-rays are directly transmitted through the reference as necessary for a clean reconstruction.

2.2. HERALDO contrast mechanism with XMLD and energy difference

The HERALDO technique reconstructs the full complex scattering amplitude of a sample from a measured interference pattern between the scattering from an object and a reference structure [14]. This is done by applying a suitable linear filter to the diffraction pattern and then taking the inverse Fourier transform [17–19], as shown schematically in Fig. 1(a).

The complex scattering factor of a sample at energy E and with polarization ϵ is

$$S_\epsilon(E) = f_{\mathrm{NR}}(\epsilon, E) + f_{\mathrm{E1}}(\epsilon, E) + \cdots . \tag{1}$$

Here, f_{NR} is the non-resonant scattering amplitude and f_{E1} is the electric dipole contribution to the resonant scattering [42], which is given as

$$f_{\mathrm{E1}} = \frac{3\hbar c}{4E}\left(F^{(0)}\delta_{ij}\epsilon_{0,i}\epsilon^{*}_{f,j} - iF^{(1)}\varepsilon_{ijk}z_i\epsilon_{0,j}\epsilon^{*}_{f,k} + F^{(2)}\delta_{i,j}\delta_{k,l}z_i z_k\epsilon_{0,j}\epsilon^{*}_{f,l}\right) \tag{2}$$

and is discussed in more detail in Supplement 1 section S1. Higher-order electric (quadrupole etc.) and magnetic transitions are typically orders of magnitude weaker and are not considered here [42]. $\hat{z} = (z_1, z_2, z_3)$ describes the orientation of the atomic magnetic moment. ϵ_0 and ϵ_f are the incident and scattered x-ray polarizations. $F^{(0,1,2)}$ are complex functions that describe the strength of the resonance; these are determined by overlap integrals between the orbitals involved in a transition and are dependent only on atomic properties [42]. Near an absorption resonance peak, both the real and imaginary parts of the scattering amplitude increase in magnitude, but tend to peak at slightly different energies [43,44]. Furthermore, the scattering amplitude depends explicitly on the x-ray polarization through the relative orientation of the x-ray polarization and the magnetic moment; this defines the magnetic contrast mechanism as discussed further in Supplement 1 section S1. For antiferromagnets, such as α-Fe_2O_3, there is a well-known relationship between the contrast and the relative orientation of the local Néel vector to the x-ray polarization axis, namely proportional to $\cos(2\theta)$ with θ the angle between the Néel vector and x-ray polarization axis [32,34,39,40]. As the real and imaginary parts of the forward scattering are related by the Kramers-Kronig relation, they will have the same polarization dependence. Hence, HERALDO images can reconstruct both the real and imaginary part of the scattering and both will be sensitive to the local Néel vector orientation, up to a sign. This is therefore directly analogous to our previous studies utilising absorptive imaging [3,32,34]. It is important to note that the difference in peak energies means that 'real' and 'imaginary' images cannot be simultaneously optimized, so that only one of them will have maximum contrast. One additional advantage of this technique is that the interference with the reference structure specifically selects the scattering in a single channel, namely that which doesn't change the polarization.

Energy-XMLD (E-XMLD) images are constructed with fixed linear x-ray polarization in the plane of the sample with normal incidence, but with diffraction patterns taken at two different energies near the Fe L_3 peaks. This works because the dichroic signal reverses sign several times across the spectrum, and one can choose energies that maximize this difference [32,34,39,40]. The contrast is defined in terms of the intensity at two energies, I_{E_1} and I_{E_2} as

$$I_{\text{E-XMLD}} = I_{\mathrm{E}_1} - I_{\mathrm{E}_2}, \tag{3}$$

referred to generally as a difference image. As the HERALDO processing is linear, one can perform the subtraction either before or after applying the filter and performing the inverse Fourier transform. Furthermore, the background intensity of each diffraction pattern is separately normalized prior to subtraction. This process ensures that images taken with HERALDO are analogous to those we studied previously through X-PEEM [3,32] or STXM [34], but with the additional feature that the primary contrast may come from either the real or imaginary part of the reconstruction. In our case, the energies chosen here were optimized to maximize the contrast in the *real* part of the HERALDO reconstruction.

Beyond the E-XMLD images discussed above, by rotating the x-ray polarization within the sample plane, one can exploit the fact that the local contrast $I_{\text{E-XMLD}} \propto \cos(2\theta)$ to reconstruct a full 2D map of the local Néel vector orientation up to a sign (Néel director field), referred to throughout as a vector map. Due to the $\cos(2\theta)$ periodicity, a set of E-XMLD images collected between 0° and 90° is in principle sufficient to achieve the full reconstruction. Our implementation of this vector mapping procedure is similar to measurements we have performed extensively using absorption-based techniques [3,32,34,45], but with the primary contrast coming from the real part of the generally complex reconstruction.

2.3. Instrumentation and measurements

X-ray holography experiments were performed on the COMET instrument at the SEXTANTS beamline, SOLEIL. Far field diffraction patterns formed via the interference of the sample and reference aperture were recorded using either a 2048x2048 pixel 16-bit PI-MTE CCD camera (Princeton instruments) placed 34 cm from the sample or a new 2048x2048 pixel sCMOS (AXIS Photonique) [46] placed 19 cm from the sample. The total exposure time was 150 s per image, comprised of a sum of many smaller snapshots. The X-ray polarization was controlled with an HU44 APPLE II undulator. X-ray energies close to the Fe L_3 edge, with a consistent gap of 0.9-1.2,eV was used for all images (see Supplement 1 Fig. S4). Magnetic fields were applied to the sample using a tunable array of 4 permanent magnet (NdFeB) rods [10]. The sample temperature was controlled with a commercial He cryostat/heater (Janis, USA) connected to the sample stage with a local flexible stripe, in principle allowing for sample temperatures 20 K-800 K [10], although only temperatures 280 K-320 K were used here. A Lakeshore 350 controller performs the temperature regulation with stability better than 100 mK. Post-processing of measured diffraction patterns, such as the application of the linear filter and inverse Fourier transform, were performed using a custom matlab script [47]. Vector maps were created from a set of ten images with different polarization angles using python (for further details, see [3,32,47]). For low-temperature vector maps ($T<T_\mathrm{M}$), OOP regions were masked out by applying a binary mask to the angular-averaged E-XMLD image, with a consistent threshold across images at the same location.

3. Results and discussion

3.1. Imaging domain walls below T_M

For $T<T_\mathrm{M}$, α-$\mathrm{Fe_2O_3}$ hosts a set of AFM domains oriented along the c-axis, related by time-reversal symmetry and connected by in-plane antiphase domain walls (ADWs) [32]. For our membranes, the c-axis is oriented OOP of the films, and as such the domains at this temperature are oriented along the x-ray k-vector in normal-incidence geometry. Therefore, E-XMLD contrast allows us to clearly distinguish between the OOP domains and the ADWs, although the pair of time-reversed OOP domains have the same contrast and so are indistinguishable.

3.1.1. Estimation of the mask resolution

Since the domain walls are narrow and their width is known from previous studies, analysis of the ADW images obtained with $T<T_\mathrm{M}$ enables us to estimate the ‘instrumental resolution’ obtained with the masks and samples as prepared here, as well as with the specific experimental configuration employed. To this end, we took a set of 10 linecuts perpendicular to domain walls imaged below T_M and performed a Gaussian fit of the pixel-by-pixel intensity, as shown in Fig. 2(a),(b). Each pixel in the reconstructed images corresponds to ~14 nm in real space, as the 3 μm diameter holes are found to be 210 pixels wide. The extracted width of the Gaussian fit to each line cut averaged 28 nm with a standard deviation of 18 nm, with larger widths found across some sections of the domain wall. This is consistent with typical domain wall sizes seen below the transition during previous X-PEEM experiments and through micromagnetic simulations [32,33,48]. Thus, the mask preparation resulted in a resolution of approximately 30 nm, which corresponds closely to the width of the reference slits as extracted from SEM images, similar to Fig. 1(d). The 14 nm pixel size was chosen based on the lateral dimensions of the camera used and the separation between the sample and detector, as the scattering vector corresponding to the furthest pixel from the image center as well as the pixel density will also ultimately limit the instrument resolution. These parameters can in principle be optimized over and above what was used in these experiments and are usually less relevant for determining the ultimate resolution of the technique than the size of the reference feature, given our current manufacturing capabilities.

3.1.2. Field-dependent behavior of the domain walls below T_M

Figure 2(c) shows an example ADW separating two OOP domains, with the associated vector map in Fig. 2(d). As discussed in our previous work, the domain walls are not homochiral and have a spatially-varying in-plane orientation [32]. The ADWs also vary slightly in width, likely due to local fluctuations in the anisotropy from inhomogeneous strain caused by defects or imprinted serendipitously during membrane transfer [34]; nonetheless, we find that the average width is consistent with our previous observations in attached thin films [32]. In addition, some small IP islands are also visible in the vector map, as often seen in such samples when the system is below T_M, resulting from the relatively weak anisotropy of the system close to the Morin transition.

Under application of magnetic fields up to 650 mT along the IP direction, the ADWs are seen to be structurally robust to change (Fig. 2(e)). This could be partly due to the higher density of defects present in α-Fe_2O_3 membranes relative to their thin-film counterparts [34]. Moreover, as the fraction of the ADW that is fully in plane is relatively small, the canted moment and associated coupling with the external field is expected to be fairly weak. Nonetheless, by analysing the vector map of the ADW (Fig. 2(f)) at 650 mT compared to the zero field case, we observe some reorientation of the IP component of the ADW. This suggests that the coupling is non-zero, and that higher fields could potentially cause complete reorientation within the ADW. Whilst this would not enforce homochirality, as the orientation relative to the domain wall vector would still spatially vary as the wall itself wound through the sample, spin reorientation within ADWs could have potential uses for racetrack-type devices, wherein ADWs perpendicular to the long axis of the racetrack are favored.

3.1.3. Imaging antiphase domain walls with circularly polarized x-rays

Interestingly, domain walls can be clearly seen for $T < T_M$ in HERALDO energy-contrast images with *circularly*-polarized x-rays (Fig. 3). We refer to these as circular x-ray magnetic energy contrast (CXMEC) images. These were taken with both left- and right-handed circular light and at the same pair of energies as the E-XMLD images and show clear contrast between the ADWs and the OOP background. The contrast is strong and very uniform within the ADWs; crucially, it is free from the variations in IP contrast observed with E-XMLD imaging, which we used to construct vector maps. Our observation of strong contrast with circular light may appear counter-intuitive, since it is generally believed that AFM textures can only be observed with linear x-ray polarization [39,40]. In fact, there is no violation of the usual rules here, since our CXMEC images were collected with a single photon helicity and are *not* circularly dichroic. Rather, the contrast simply arises from the different scattering of circular light for OOP vs IP magnetic moments, as discussed further in Supplement 1 section S1. By symmetry, this imaging methodology is insensitive to the IP direction within the ADWs, which is both an advantage and a disadvantage, the latter obviously being that one cannot construct vector maps. A significant advantage is that the ADW can be seen in its entirety with a single polarization setting, without the characteristic null-contrast 'breaks' observed with E-XMLD (e.g., in Fig. 2). Overall, CXMEC appears to be a valuable addition to the imaging 'toolkit' for antiferromagnets.

3.2. Imaging domains above T_M

After warming the sample through T_M and up to 320 K, we expected the ADWs to widen and form an IP matrix of 3-fold domains separated by 120° and their time-reversed counterparts, akin to what was observed previously in thin films [32]. Indeed, our E-XMLD HERALDO images change drastically compared to low temperature. At 320 K and zero magnetic field, a domain is clearly visible in single-polarization images (Fig. 4(a)). Performing an E-XMLD vector map by rotating the polarization of the incident beam allows us to map the three pairs of 120° domains (Fig. 4(d)), and to identify the original domain wall as a narrow 'blue' band (Néel vector 'right' or 'left' with respect to the Fig.). The relatively weak basal plane anisotropy means that the

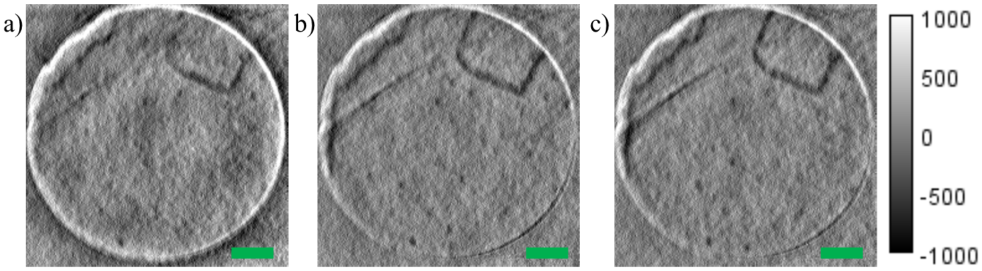

Fig. 3. a) Holographic E-XMLD image of ADWs for $T < T_{\mathrm{M}}$. b,c) CXMEC image of the same ADWs using b) circular left and c) circular right polarized x-rays. Green scale bars are 500 nm.

domain structure deviates significantly from an ideal triaxial distribution (see Supplement 1 Fig. S6). As previously explained, each domain is indistinguishable from its time-reversed counterpart, due to the inherent 180° periodicity in this technique. In the center of the figure, the 'blue' domain appears to be pinched and connect two pairs of green/red domains, which are likely to be time-reversed counterparts (green/anti-green and red/anti-red).

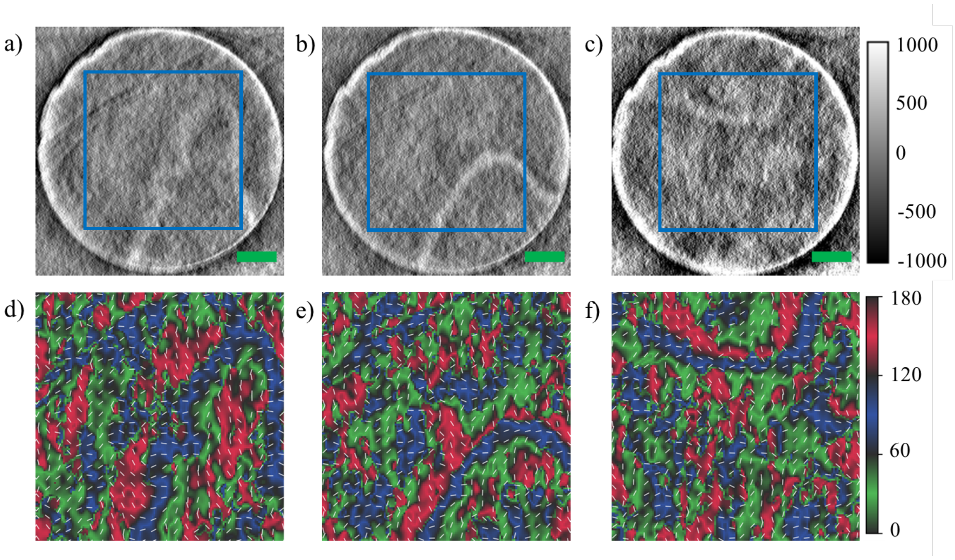

Fig. 4. (a-c) Holographic E-XMLD images of AFM domains taken at different field values for the same sample position as Fig. 2 after warming to 320 K (above T_{M}). (d-f) corresponding vector maps taken in the blue boxed regions in (a-c). (a,d) correspond to the zero-field state and (b,e) were taken with a 550 mT steady-state field applied to the right of the image. (c,f) are taken with the field reversed along the horizontal direction with a strength of 400 mT. Green scale bars are 500 nm. The white bars in the vector maps show the local Néel vector orientation.

Under application of a 550 mT IP field along the horizontal direction, the domains changes drastically, as clearly evidenced in the vector map (Fig. 4(e)). In particular, the area enclosed by the narrow 'blue' domain is seen to shrink significantly with respect to zero field. Due to beamtime constraints, the magnetic field was applied in steps without any intermediate imaging. Therefore, it is difficult to tell from the vector map alone whether this corresponded to a movement of the 'blue' domain towards the bottom right corner or to fracturing into several smaller domains.

Moreover, there is a large-scale redistribution of the domains compared to the zero-field case. As the field is applied horizontally relative to the displayed images (with a positive field towards the right) and since the canted moment of a given domain is perpendicular to its Néel vector, one would expect 'blue' domains to have minimal coupling to the applied field, whereas 'green' and 'red' domains should both couple equally. Rather than the 'blue' domain contracting, therefore, it is more likely that the 'red'/'green' domains inside couple negatively with the applied field and so shrink, whereas those outside couple positively and therefore expand. Here, an important observation is that the applied field provides a symmetry-breaker between the otherwise indistinguishable time-reversed domain pairs, which have opposite canted moment and therefore are favored/disfavored (respectively) in the presence of an applied field. Hence, any newly nucleated domains must have canted magnetic moment parallel to the applied field, whereas the shrunken domains must be their time-reversed counterparts. The blue domains largely serve as pathways for this domain repopulation, as this pair of domains are roughly equal in energy with respect to the applied field. A similar trend (in reverse) is evident when the field direction is reversed (Fig. 4(c),(f)). Our data clearly demonstrate that, given enough data collection time, one could reconstruct in detail the evolution of the AFM texture *in situ* as a function of magnetic field, temperature or in indeed other external parameters such as uniaxial/biaxial strain [34].

3.3. Topological textures in magnetic fields

Similar to what was observed in our previous studies on attached thin films and freestanding AFM membranes using X-PEEM [3,32] and STXM [34], respectively, topological textures were also found to be stable (although seemingly less abundant) in the membranes prepared for this holography experiment. Both a single E-XMLD image and the associated vector map for a pair of topological textures are shown in Fig. 5, taken at 320 K in the absence of an applied field. A meron and an antimeron, shown by a yellow circle and a blue square respectively, are clearly present in the image, as determined by the winding of red/blue/green domains around the core. The meron and antimeron in the pair are separated spatially by ≈ 1.7 μm, much further than the magnetic exchange length of the system (≈ 100 nm [33]) and therefore they should not be categorized as a bound bimeron system. As for all E-XMLD-based techniques, we are not directly sensitive to the topological charge $\boldsymbol{q}$, and we cannot determine whether the pair is trivial ($\boldsymbol{q} = 0$) or topological ($\boldsymbol{q} = \pm 1$) [33]. This provides a direct verification of the results and conclusions of our previous studies on recently developed crystalline antiferromagnetic membranes [34].

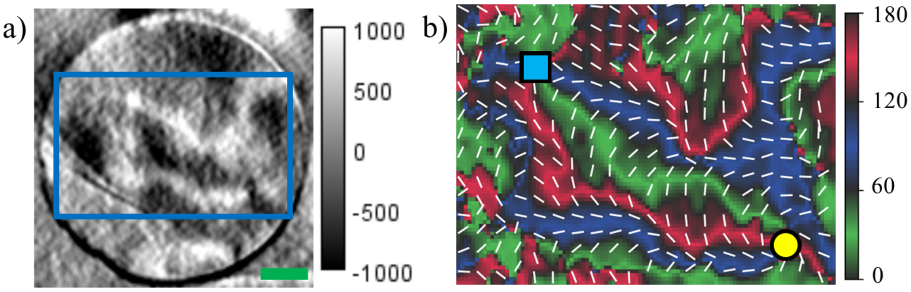

Fig. 5. (a) Holographic E-XMLD image and (b) corresponding vector map of topological textures in the absence of an applied field. The vector map is taken in the blue boxed region in (a). Green scale bar is 500 nm.

Under application of a 500 mT magnetic field in the IP direction towards the right (as shown in Fig. 5) to the pair of topological textures, we observe an obvious shrinking of the domains connecting the two cores, as seen in Fig. 6(b) compared to the initial zero field state (Fig. 6(a)).

This appears to be a largely reversible change, since reducing the field down to 100 mT returns the domains roughly the original position (Fig. 6(c)). A further cycle to 500 mT and back shows an almost identical behavior (Fig. 6(d),(e)). This suggests that the main effect that these fields have on topological textures is to alter the energy landscape and thereby modify the proportion of each domain ‘flavor’, whilst preserving the overall winding structure around the topological cores, as discussed below. The almost exact reproducibility under field cycles is probably the result of defect pinning of the topological textures and domain structures, making it more energetically favorable for them to return to their original positions when the applied field is removed. This emphasizes the topological protection inherent to the textures, as well as the inherent immunity to applied fields often stated as one of the primary benefits of antiferromagnets for spintronics applications.

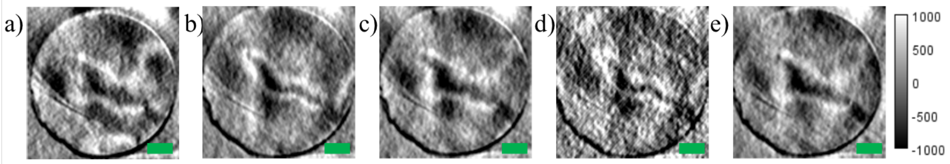

Fig. 6. Holographic E-XMLD images taken at the position of the pair of topological textures shown in Fig. 5 as a function of field, cycling to 500 mT and back down to 100 mT twice. The sequence is: (a) 0 mT initial state, (b) 500 mT, (c) 100 mT, (d) 500 mT, and (e) 100 mT. The lighter regions correspond to the blue domains connecting the two topological cores shown in the vector map above. Green scale bars are 500 nm.

3.3.1. Qualitative model of a meron-antimeron pair in applied field

The observed shrinkage of certain domains connecting the meron to the antimeron in applied field is clearly due to the fact that some of the domains are less energetically favorable in the presence of the field and therefore shrink. For example, let us assume that the initial configuration around the meron core is $R - \bar{G} - B - \bar{R} - G - \bar{B}$ as in Fig. 5, with barred domains being the time-reversed counterpart of the unbarred domain ($\bar{R}$= anti-red), and let us also assume that the angular range of each domain is roughly the same in zero field. Let the weak magnetization of the $B/\bar{B}$ domain be close to the positive/negative y axis, respectively (Néel vector along the positive/negative x axis). Then, upon application of a magnetic field along the positive x direction, we expect the configuration to become $\boldsymbol{R} - \boldsymbol{\bar{G}} - B - \bar{r} - g - \bar{B}$, where bold/lowercase symbol indicate greater/lower angular range for a given domain. The effect will be maximal for domains with the weak magnetization oriented parallel/antiparallel to the field. This qualitative scenario is entirely compatible with our observations in Fig. 6, and could be further confirmed by performing full vector maps as in Fig. 5 at each field.

4. Conclusions

We have presented the first example of holographic imaging of antiferromagnetic domains, utilising energy-contrast x-ray magnetic linear dichroism (E-XMLD) and energy-contrast magnetic imaging with circularly polarized x-rays (CXMEC) in α-Fe_2O_3 membranes. As part of this study, we have produced detailed director-field maps of the Néel vector based on E-XMLD as well as sharp antiphase domain wall (ADW) images using CXMEC. Our results confirm the presence of topological textures in α-Fe_2O_3 membranes and demonstrate how these textures evolve in the presence of an applied magnetic field. More specifically, we demonstrated cyclic, field dependent evolution of AFM domains in α-Fe_2O_3 due to the coupling between the field and the canted moment. More broadly, we have shown that E-XMLD/CXMEC HERALDO are promising techniques for imaging-based investigations of a wide range of AFM materials with *in-situ* perturbations, including temperature control and magnetic field. This work opens way for investigations of other AFM materials as well as the simultaneous application of additional *in situ* tuning parameters such as electric fields, laser pulses, and uniaxial/biaxial strain.

Funding. Engineering and Physical Sciences Research Council (2285094, DTP: 2285094, EP/M020517/1, EP/X024938/1); Ministry of Education - Singapore (MOE-T2EP50120-0015); Agency for Science, Technology and Research (A1983c0034, A2083c0054); National Research Foundation Singapore (NRF2020-NRF-ISF004-3518).

Acknowledgments. Work done at the University of Oxford was supported by Engineering and Physical Sciences Research Council (EPSRC) (EP/M020517/1) and the Oxford-ShanghaiTech collaboration project. J.H. was supported by the EPSRC (DTP Grant No. 2285094). H.J. acknowledges the support of Marie Skłodowska-Curie Postdoctoral Fellowship under the UK Research and Innovation Horizon Europe Guarantee Funding (EP/X024938/1). H.J., J.X.H., and A.A. acknowledge the funding support from the Ministry of Education (MOE) Singapore under the Academic Research Fund Tier 2 (Grant No. MOE-T2EP50120-0015), the Agency for Science, Technology and Research (A*STAR) under its Advanced Manufacturing and Engineering (AME) Individual Research Grant (IRG) (Grants No. A1983c0034 & A2083c0054), and the National Research Foundation (NRF) of Singapore under its NRF-ISF joint program (Grant No. NRF2020-NRF-ISF004-3518). We acknowledge SOLEIL for provision of synchrotron radiation facilities at the SEXTANTS beamline under the projects 20200283 and 20210750.

Disclosures. The authors declare no conflicts of interest.

Data availability. Data that support the findings of this study are available from the corresponding author upon reasonable request.

Supplemental document. See Supplement 1 for supporting content.

References

1. A. Sakdinawat and D. Attwood, "Nanoscale x-ray imaging," Nat. Photonics **4**(12), 840–848 (2010).
2. Z. Luo, A. Hrabec, T. P. Dao, *et al.*, "Current-driven magnetic domain-wall logic," Nature **579**(7798), 214–218 (2020).
3. F. P. Chmiel, N. Waterfield-Price, R. D. Johnson, *et al.*, "Observation of magnetic vortex pairs at room temperature in a planar α -Fe$_2$ O$_3$/Co heterostructure," Nat. Mater. **17**(7), 581–585 (2018).
4. N. Waterfield Price, R. D. Johnson, W. Saenrang, *et al.*, "Electrical switching of magnetic polarity in a multiferroic BiFeO$_3$ device at room temperature," Phys. Rev. Appl. **8**(1), 014033 (2017).
5. M. G. Kim, H. Miao, B. Gao, *et al.*, "Imaging antiferromagnetic antiphase domain boundaries using magnetic bragg diffraction phase contrast," Nat. Commun. **9**(1), 5013 (2018).
6. S. Finizio, S. Wintz, E. Kirk, *et al.*, "In situ membrane bending setup for strain-dependent scanning transmission x-ray microscopy investigations," Rev. Sci. Instrum. **87**(12), 123703 (2016).
7. O. J. Amin, S. F. Poole, S. Reimers, *et al.*, "Antiferromagnetic half-skyrmions electrically generated and controlled at room temperature," Nat. Nanotechnol. **18**(8), 849–853 (2023).
8. F. Büttner, M. A. Mawass, J. Bauer, *et al.*, "Thermal nucleation and high-resolution imaging of submicrometer magnetic bubbles in thin thulium iron garnet films with perpendicular anisotropy," Phys. Rev. Mater. **4**, 011401 (2020).
9. A. Sala, M. Rocca, T. S. Rahman, *et al.*, *Imaging at the Mesoscale (LEEM, PEEM)* (Springer International Publishing, 2020), pp. 387–425.
10. H. Popescu, J. Perron, B. Pilette, *et al.*, "Comet: a new end-station at soleil for coherent magnetic scattering in transmission," J. Synchrotron Radiat. **26**(1), 280–290 (2019).
11. D. H. Bilderback, P. Elleaume, and E. Weckert, "Review of third and next generation synchrotron light sources," J. Phys. B **38**(9), S773–S797 (2005).
12. S. Shin, "New era of synchrotron radiation: fourth-generation storage ring," AAPPS Bull. **31**(1), 21 (2021).
13. T. Wang, D. Zhu, B. Wu, *et al.*, "Femtosecond single-shot imaging of nanoscale ferromagnetic order in co/pd multilayers using resonant x-ray holography," Phys. Rev. Lett. **108**(26), 267403 (2012).
14. S. Mustafi and T. Latychevskaia, "Fourier transform holography: A lensless imaging technique, its principles and applications," Photonics **10**(2), 153 (2023).
15. F. Pfeiffer, "X-ray ptychography," Nat. Photonics **12**(1), 9–17 (2018).
16. R. Battistelli, D. Metternich, M. Schneider, *et al.*, "Coherent x-ray magnetic imaging with 5 nm resolution," (2023).
17. M. Guizar-Sicairos and J. R. Fienup, "Holography with extended reference by autocorrelation linear differential operation," Opt. Express **15**(26), 17592 (2007).
18. M. Guizar-Sicairos and J. R. Fienup, "Direct image reconstruction from a fourier intensity pattern using heraldo," Opt. Lett. **33**(22), 2668 (2008).
19. T. A. Duckworth, F. Ogrin, S. S. Dhesi, *et al.*, "Magnetic imaging by x-ray holography using extended references," Opt. Express **19**(17), 16223 (2011).
20. J. C. Loudon, A. C. Twitchett-Harrison, D. C.-O. no, *et al.*, "Do images of biskyrmions show type-ii bubbles?" Adv. Mater. **31**(16), 1806598 (2019).

21. L. A. Turnbull, M. T. Birch, A. Laurenson, *et al.*, “Tilted x-ray holography of magnetic bubbles in mnniga lamellae,” ACS Nano **15**(1), 387–395 (2021).
22. N. Bukin, C. McKeever, E. Burgos-Parra, *et al.*, “Time-resolved imaging of magnetic vortex dynamics using holography with extended reference autocorrelation by linear differential operator,” Sci. Rep. **6**(1), 36307 (2016).
23. M. D. P. Martínez, A. Wartelle, C. H. Martínez, *et al.*, “Three-dimensional tomographic imaging of the magnetization vector field using fourier transform holography,” Phys. Rev. B **107**(9), 094425 (2023).
24. R. Lebrun, A. Ross, S. A. Bender, *et al.*, “Electrically tunable long-distance transport in crystalline antiferromagnetic iron oxide,” Nature **561**(7722), 222–225 (2018).
25. R. Lebrun, A. Ross, O. Gomonay, *et al.*, “Long-distance spin-transport across the Morin phase transition up to room temperature in ultra-low damping single crystals of the antiferromagnet α -Fe$_2$ O$_3$,” Nat. Commun. **11**(1), 6332 (2020).
26. R. Lebrun, A. Ross, O. Gomonay, *et al.*, “Anisotropies and magnetic phase transitions in insulating antiferromagnets determined by a spin-Hall magnetoresistance probe,” Commun. Phys. **2**(1), 50 (2019).
27. J. Fischer, M. Althammer, N. Vlietstra, *et al.*, “Large spin Hall magnetoresistance in antiferromagnetic α -Fe$_2$ O$_3$/Pt heterostructures,” Phys. Rev. Appl. **13**(1), 014019 (2020).
28. H. Jani, J. Linghu, S. Hooda, *et al.*, “Reversible hydrogen control of antiferromagnetic anisotropy in α -Fe$_2$ O$_3$,” Nat. Commun. **12**(1), 1668 (2021).
29. Z. S. Lim, H. Jani, T. Venkatesan, *et al.*, “Skyrmionics in correlated oxides,” MRS Bull. **46**(11), 1053–1062 (2021).
30. A. H. Morrish, *Canted Antiferromagnetism: Hematite* (World Scientific, 1994).
31. F. J. Morin, “Magnetic susceptibility of α -Fe$_2$ O$_3$ and α -Fe$_2$ O$_3$ with added titanium,” Phys. Rev. **78**(6), 819–820 (1950).
32. H. Jani, J.-C. Lin, J. Chen, *et al.*, “Antiferromagnetic half-skyrmions and bimerons at room temperature,” Nature **590**(7844), 74–79 (2021).
33. J. Harrison, H. Jani, and P. G. Radaelli, “Route towards stable homochiral topological textures in a-type antiferromagnets,” Phys. Rev. B **105**(22), 224424 (2022).
34. H. Jani, J. Harrison, S. Hooda, *et al.*, “Spatially reconfigurable antiferromagnetic states in topologically rich free-standing nanomembranes,” *Nat. Mater.* (2024).
35. T. W. B. Kibble, “Topology of cosmic domains and strings,” J. Phys. A: Math. Gen. **9**(8), 1387–1398 (1976).
36. W. H. Zurek, “Cosmological experiments in superfluid helium?” Nature **317**(6037), 505–508 (1985).
37. A. del Campo and W. H. Zurek, “Universality of phase transition dynamics: topological defects from symmetry breaking,” Int. J. Mod. Phys. A **29**(08), 1430018 (2014).
38. A. K. C. Tan, H. Jani, M. Högen, *et al.*, “Revealing emergent magnetic charge in an antiferromagnet with diamond quantum magnetometry,” Nat. Mater. **23**, 205–211 (2024).
39. P. Kuiper, B. G. Searle, P. Rudolf, *et al.*, “X-ray magnetic dichroism of antiferromagnetic Fe$_2$O$_3$: the orientation of magnetic moments observed by fe 2p x-ray absorption spectroscopy,” Phys. Rev. Lett. **70**(10), 1549–1552 (1993).
40. E. Arenholz, G. V. der Laan, R. V. Chopdekar, *et al.*, “Anisotropic x-ray magnetic linear dichroism at the Fe L$_{2,3}$ edges in -Fe$_3$ O$_4$,” Phys. Rev. B **74**(9), 094407 (2006).
41. “X-ray attenuation length calculator,” https://henke.lbl.gov/optical_constants/atten2.html. Last accessed: 2024-01-02.
42. J. P. Hill and D. F. McMorrow, “Resonant exchange scattering: Polarization dependence and correlation function,” Acta Crystallogr. Sect. A **52**(2), 236–244 (1996).
43. A. Scherz, W. F. Schlotter, K. Chen, *et al.*, “Magnetic imaging at linearly polarized x-ray sources,” Opt. Express **18**(13), 13608–13615 (2010).
44. M. Sacchi, H. Popescu, N. Jaouen, *et al.*, “Magnetic imaging by fourier transform holography using linearly polarized x-rays,” Opt. Express **20**(9), 9769–9776 (2012).
45. N. Waterfield Price, R. D. Johnson, W. Saenrang, *et al.*, “Coherent magnetoelastic domains in multiferroic BiFeO$_3$ films,” Phys. Rev. Lett. **117**(17), 177601 (2016).
46. K. Desjardins, K. Medjoubi, M. Sacchi, *et al.*, “Backside-illuminated scientific cmos detector for soft x-ray resonant scattering and ptychography,” J. Synchr. Rad. **27**(6), 1577–1589 (2020).
47. All data and analysis scripts will be uploaded to the Oxford repository upon publication, https://ora.ox.ac.uk/.
48. P. G. Radaelli, J. Radaelli, N. Waterfield-Price, *et al.*, “Micromagnetic modeling and imaging of vortex vertical bar meron structures in an oxide vertical bar metal heterostructure,” Phys. Rev. B **101**(14), 144420 (2020).